

# Inverse Design of Nanophotonic Color Router Robust to Oblique Incidence

Jaehyun Jeon, Chanhyung Park, Doyoung Heo, Haejun Chung, and Min Seok Jang\*

With continued pixel miniaturization, conventional micro-lenses and absorptive color filters in CMOS image sensors suffer from significant performance degradation and low photon influx as the pixel pitch approaches the diffraction limit. While numerous studies have explored nanophotonic color routers as a solution, most lack a systematic analysis of optical efficiency under broad incident angles, which is critical for practical CIS applications. In this work, an inverse design framework based on automatic differentiation is developed to achieve robustness against incident angle variations. The design maintains a high optical efficiency of 78% on average within a  $\pm 12^\circ$  incident angle range for unpolarized light. The trade-off relation between the acceptance angle range and the achievable optical efficiency of the device is also identified. The proposed optimized method is then demonstrated and can be further extended to design broadband broad-angle color routers. These findings pave the way for more efficient and versatile CMOS image sensors, offering substantial improvements over existing methods by ensuring efficient light utilization under realistic illumination conditions.

With continued pixel miniaturization in CMOS image sensors, pixel sizes of commercial CIS have reached as small as  $0.5 \mu\text{m}$ .<sup>[9]</sup> However, as pixel dimensions enter the subwavelength regime, conventional optical components encounter fundamental limitations. This miniaturization has led to severe performance degradation in traditional CIS systems, particularly in the performance of the micro-lens array as the operating regime shifts from ray optics to wave optics.<sup>[10–13]</sup> In addition, absorptive color filters inherently discard a significant portion of incident light, limiting the maximum optical efficiency to 25% for red and blue pixels, and 50% for green. As the pixel area decreases, the available photon flux scales down proportionally, making this intrinsic energy loss a fundamental limitation to further downscaling.

To address these challenges, nanophotonic color routers based on optical metastructures have been proposed as alternatives to conventional microlens arrays and absorptive color filters.<sup>[14–26]</sup> These color routers guide incident light to the appropriate subpixels depending on its wavelength by multiple scattering within a complex subwavelength-scale structure. This approach not only offers ultracompact designs for subwavelength-scale pixels but also addresses the inefficiency of conventional CIS systems, where light directed on nontarget subpixels is wasted.

Significant progress has been made in the design of nanophotonic color routers that effectively route light based on its wavelength. Among various architectures, freeform nanophotonic color routers, which are unconstrained by a fixed topology,<sup>[27]</sup> have demonstrated superior performance, including near-perfect optical efficiency,<sup>[15,16]</sup> single-layer operation,<sup>[19–23]</sup> and multifunctional capabilities<sup>[14,25]</sup> through various design methods. These high-performance structures typically require a high degree of freedom, and are commonly designed using advanced optimization methods,<sup>[28]</sup> including nature-inspired heuristics such as genetic algorithms (GA)<sup>[22–24]</sup> and particle swarm optimization (PSO),<sup>[26]</sup> and gradient-based methods using automatic differentiation (AD)<sup>[21]</sup> and adjoint variables.<sup>[14–16]</sup> In particular, inverse design frameworks based on AD and adjoint variable methods have proven effective in exploring large and complex design spaces, efficiently finding optimal device structures.<sup>[15,16,29]</sup>

Despite these advances, most prior works have focused exclusively on normal incidence of light, neglecting the angular

## 1. Introduction

CMOS image sensors (CIS) are core components in modern imaging systems, converting analog optical signals into digital information with a spatial resolution approaching the diffraction limit.<sup>[1]</sup> These image sensors have been widely used in applications requiring spectral and spatial light analysis, such as hyperspectral imaging,<sup>[2,3]</sup> spectroscopy,<sup>[4,5]</sup> and computational vision.<sup>[6,7]</sup> To capture color information, CIS typically consists of a micro-lens array, a color filter array (CFA), and photodetectors arranged in a Bayer pattern.<sup>[8]</sup> The micro-lens array focuses incident light onto each subpixel, while the CFA absorbs unwanted wavelengths, allowing only the designated spectral band to reach each detector.

J. Jeon, C. Park, D. Heo, M. S. Jang  
School of Electrical Engineering  
Korea Advanced Institute of Science and Technology  
Daejeon 34141, Republic of Korea  
E-mail: jang.minseok@kaist.ac.kr

H. Chung  
Graduate School of Artificial Intelligence Semiconductor  
Hanyang University  
Seoul 04763, Republic of Korea

 The ORCID identification number(s) for the author(s) of this article can be found under <https://doi.org/10.1002/adom.202501697>

DOI: 10.1002/adom.202501697

variation that arises in commercial CIS. In practical CIS applications, the incident angle of incoming light cannot be assumed to be perfectly normal, as they are used for imaging systems with finite  $f$ -numbers. Previous studies report that acceptance angles of typical commercial sensors often range from  $8^\circ$  to  $11^\circ$  for  $f/2.4$  to  $f/1.7$  lenses in  $\text{SiO}_2$ <sup>[14,30]</sup> and can further increase as the numerical aperture (NA) of the imaging system increases,<sup>[31,32]</sup> depending on the pixel pitch, lens type, and stacking architecture. As a result, the performance of many existing designs degrades significantly under off-normal illumination, revealing a critical gap in achieving angular robustness. Addressing this limitation requires optimization strategies that explicitly incorporate oblique incidence conditions into the design process.

In this study, we present an angle-tolerant nanophotonic color router designed with a gradient-based optimization method based on rigorous coupled-wave analysis (RCWA). By incorporating oblique incidence into the objective function and leveraging a diagonal symmetry, we achieve over 78% average optical efficiency within a  $\pm 12^\circ$  incident angle range with minimal inter-subpixel crosstalk of 12% for unpolarized illumination. We further investigate how the performance varies with the acceptance angle range and the number of layers ( $N_L$ ) composing the color router, highlighting the role of structural degrees of freedom in setting angular performance limits. Finally, we show that our device optimization scheme can be extended to design angle-robust color routers for broadband operation. Unlike previous works that partly discussed the issue of non-normal incidence,<sup>[14–16]</sup> our work constitutes a design framework that enforces the robustness against incidence angle variation and thereby provides a systematic analysis on how the angle-robustness depends on the design parameters, exploring the intrinsic performance limit by employing freeform structures with high degrees of freedom.

## 2. Design Strategy

Nanophotonic color routers replace the traditional roles of microlenses and dye-absorptive filters by simultaneously redirecting the incident light into its corresponding subpixel depending on wavelength. This functionality is achieved through multiple scattering and propagation phase variations dictated by the spatial distribution of refractive indices. To this end, we structure the design region above a Si photodetector into a large number of nanoscale voxels in the form of square pillars, as illustrated in **Figure 1a**. The design region is configured as a square column with a lateral dimension of  $1\ \mu\text{m}$  and a height of  $2\ \mu\text{m}$ . This column is discretized into a pixelated array, where each layer consists of  $50 \times 50$  independent voxels. Vertically, the structure is composed of  $N_L = 100$  layers, forming a highly resolved 3D grid. Each voxel within this grid is filled with either of the two distinct CMOS-compatible materials, silicon nitride ( $\text{Si}_3\text{N}_4$ ) and silicon dioxide ( $\text{SiO}_2$ ).

To ensure consistent optical efficiency for azimuthal angles of both  $0^\circ$  and  $90^\circ$ , a diagonal symmetry condition of  $n(x, y) = n(y, x)$  is imposed on the refractive index distribution as illustrated in **Figure 1b**. This condition not only enhances performance at these specific azimuthal angles but also guarantees identical optical responses under TE and TM polarizations at normal incidence, which is crucial for polarization-independent operation. Additionally, the symmetry ensures that the two green subpixels

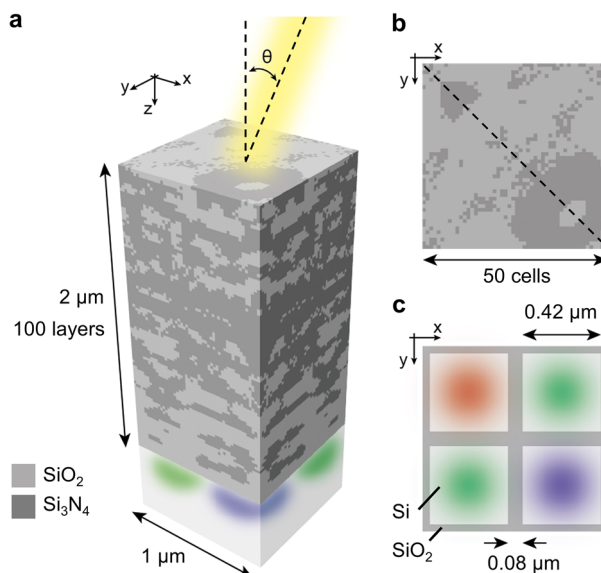


**Figure 1.** Nanophotonic color router robust to oblique incidence. a) Illustration of nanophotonic color routing under oblique incidence. The  $1\ \mu\text{m} \times 1\ \mu\text{m} \times 2\ \mu\text{m}$  design region is divided into  $50 \times 50 \times 100$  voxels, which are filled with either  $\text{SiO}_2$  (light gray) or  $\text{Si}_3\text{N}_4$  (dark gray). The structure is optimized for incident angles within  $\pm 12^\circ$ . b) Top view of the design region, where the dashed line indicates the symmetry plane for  $n(x, y) = n(y, x)$ . c) Cross-sectional view of the pixelated photodetectors with the Bayer arrangement indicated by colors. The Si photosensitive areas are  $0.42\ \mu\text{m}$  wide and surrounded by  $0.08\ \mu\text{m}$  wide  $\text{SiO}_2$  deep trench isolation.

in the Bayer pattern exhibit similar efficiency, preserving spatial color balance. **Figure 1c** shows the photodetector positioned directly beneath the design region, consisting of four photosensitive silicon subpixels arranged in a Bayer pattern within a square configuration, surrounded by deep trench isolation walls with  $\text{SiO}_2$ . The active region of each subpixel has a width of  $0.42\ \mu\text{m}$ , which is similar to or shorter than the wavelength of visible light.

The enormous degrees of design freedom,  $N \cong 50 \times 50 \times 100 / 2 = 125,000$ , are beyond the capacity of classical global optimization methods such as GA<sup>[33]</sup> or PSO.<sup>[34]</sup> Here, we employ a gradient-based local optimization framework integrated with AD, which enables efficient model refinement by iteratively updating parameters using AD-computed gradients.<sup>[35,36]</sup> AD operates by recording the computational path during the forward simulation and subsequently applying the chain rule to efficiently compute gradients during the backward pass.<sup>[37,38]</sup> Unlike the conventional finite-difference method, whose gradient computation time scales with the number of design variables, AD allows for obtaining the figure of merit (FoM) gradient on an arbitrary number of variables in a short time.

The detailed optimization procedure is illustrated in **Figure 2**. In the optimization process, the design parameters  $p_{ijk}$ , which determine the refractive indices  $n_{ijk}$  of each voxel in the 3D structure are used to construct the device geometry. To enforce structural symmetry across the  $y = x$  plane, only one half of the symmetric region is independently parameterized, while the other half is mirrored such that  $p_{ijk} = p_{jik}$ , as indicated in **Figure 2**. The initial values of  $p_{ijk}$  are randomly assigned within  $(-\infty, \infty)$ , and then normalized to values between 0 and 1 with a sigmoid

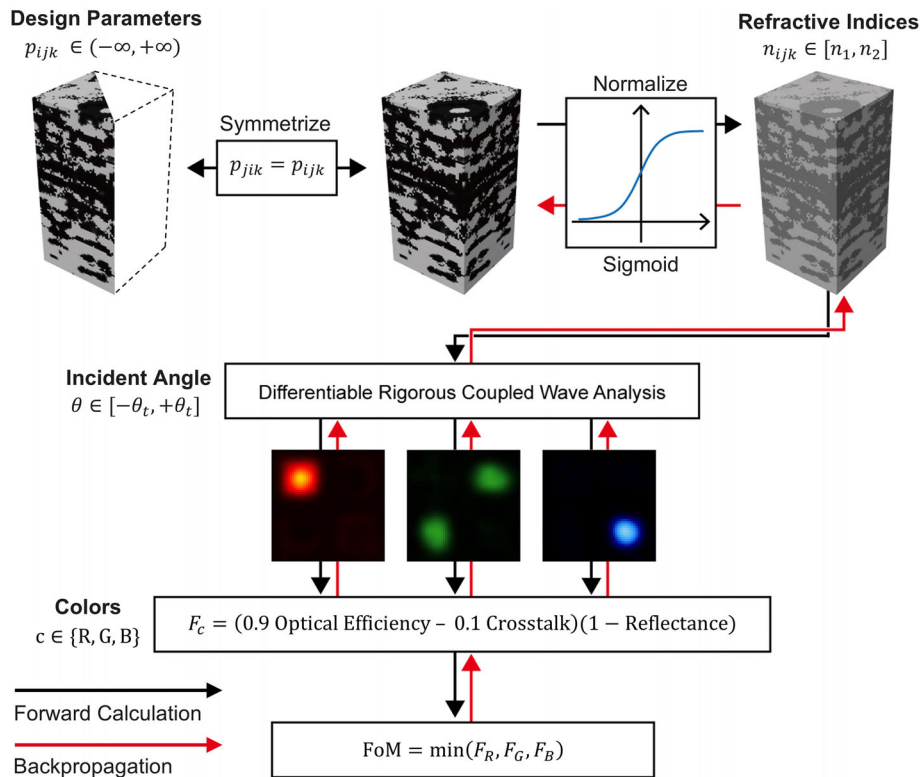


**Figure 2.** Optimization flow chart for nanophotonic color router design. The optimization process involves calculating the figure of merit through the black arrows and performing backpropagation based on partial derivatives, following red arrows, to refine the latent matrix. Normalization is applied to the latent matrix to adjust each voxel's refractive index between those of silicon nitride and silicon oxide. The electromagnetic field is evaluated with differentiable rigorous coupled wave analysis, with the condition of the incident angle within  $\pm \theta_t$ .

function. These normalized values are mapped to the refractive index range  $[n_1, n_2]$ , where values near 0 and 1 correspond to  $\text{SiO}_2$  and  $\text{Si}_3\text{N}_4$ , respectively. Intermediate values represent effective media between the two. We note that  $n_1(\lambda)$  and  $n_2(\lambda)$  take into account for the realistic wavelength dependence of refractive indices across the RGB spectral bands.<sup>[39,40]</sup>

For a given refractive index distribution, the electromagnetic field of the nanophotonic color router is computed through a rigorous coupled-wave analysis (RCWA) using MEENT, a PyTorch-based RCWA library that supports AD.<sup>[41]</sup> The optical efficiency (OE) is defined as the ratio of the z-directional Poynting vector,  $S_z$ , integrated over the target photodetector region to the total incident power, where  $(x_{i1}, x_{i2})$  and  $(y_{i1}, y_{i2})$  define the spatial boundaries of the subpixel corresponding to the target color  $i \in \{R, G, B\}$ . The total incident power is calculated by integrating the incident  $S_z$  over the entire unit cell area of size  $L \times L$ , where  $L = 1 \mu\text{m}$  denotes the periodicity of the structure.

$$\text{OE}(\theta, \lambda) = \frac{\int_{y_{i1}}^{y_{i2}} \int_{x_{i1}}^{x_{i2}} S_z(\lambda) |_{z=2\mu\text{m}} dx dy}{\int_0^L \int_0^L S_z(\lambda) |_{\text{inc}} dx dy} \quad (1)$$

The optical crosstalk (OX) is defined as the ratio of power flux misrouted to nontarget photodetector regions  $j \neq i$  as follows:

$$\text{OX}(\theta, \lambda) = \frac{\sum_{j \neq i} \int_{y_{j1}}^{y_{j2}} \int_{x_{j1}}^{x_{j2}} S_z(\lambda) |_{z=2\mu\text{m}} dx dy}{\int_0^L \int_0^L S_z(\lambda) |_{\text{inc}} dx dy} \quad (2)$$

The monochromatic performance ( $F$ ) is evaluated as a weighted sum of optical efficiency and optical crosstalk under a specific incident angle ( $\theta$ ) and wavelength, multiplied by  $1 - R(\theta, \lambda)$  to account for the reflectance ( $R$ ) loss<sup>[16,24]</sup> as follows:

$$F(\theta, \lambda) = (0.9 \text{ OE}(\theta, \lambda) - 0.1 \text{ OX}(\theta, \lambda)) \times (1 - R(\theta, \lambda)) \quad (3)$$

FoM is completed by incorporating the minimum value of  $F$  among the three wavelengths, which correspond to the center wavelength of R, G, and B: 650, 550, and 450 nm, respectively. This minimax algorithm optimizes for the worst-performing wavelength, ensuring uniform optical efficiency across a broad wavelength range. During the optimization process, each voxel's refractive index continuously varies within the range defined by the refractive indices of  $\text{Si}_3\text{N}_4$  and  $\text{SiO}_2$ . During the optimization, the refractive index distribution gradually converges to the target material values ( $\text{Si}_3\text{N}_4$  and  $\text{SiO}_2$ ). However, for practical fabrication, each voxel should be rounded to either  $\text{Si}_3\text{N}_4$  or  $\text{SiO}_2$ , as intermediate values are not physically realizable. However, for practical fabrication, each voxel must be rounded to either  $\text{Si}_3\text{N}_4$  or  $\text{SiO}_2$ , as intermediate values are not physically realizable. Therefore, a final binarization step is applied after the optimization is complete. In this step, all remaining voxels with intermediate refractive indices are rounded to the nearest material value.

To achieve a color router with enhanced robustness against oblique incidence, we optimized the structure by iteratively varying the incident angle during the design process. In each

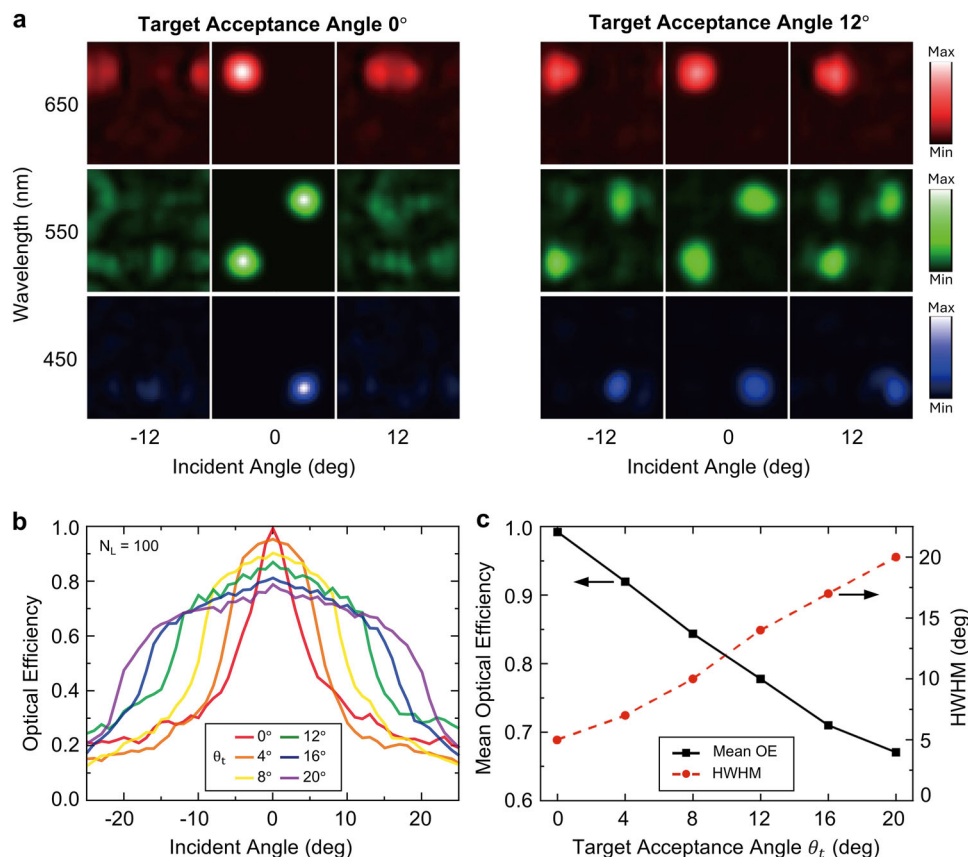


**Figure 3.** Performance of optimized color router. a) Comparison of the performance between structures considering and not considering oblique incidence. The field distributions of the z-direction Poynting vector at the top of the photodetector are shown for each wavelength and incident angle condition. The left and right sides represent the structure optimized with  $\theta_t$  of 0° and 12°, respectively. b) The average of the RGB optical efficiencies of optimized structures for different  $\theta_t$ . c) The Pareto front of the optimized structure's performance, showing the trade-off between HWHM and mean optical efficiency. The x-axis indicates the target acceptance angle ( $\theta_t$ ) used during optimization. The mean optical efficiency is represented by the black line, and the HWHM value is represented by the red dashed line.

iteration, a single incident angle is selected from the target incidence angles spanning from  $-\theta_t$  to  $\theta_t$  in 2° increments and used in the simulation. We set the target acceptance angle  $\theta_t$  to 12°, which is compatible with a wide range of practical applications while avoiding excessive trade-offs in device performance. This range strikes a balance between practical relevance and design feasibility, ensuring angular robustness under realistic illumination scenarios. To ensure polarization insensitivity under oblique incidence, both TE and TM polarizations are simulated at each selected angle, and the resulting optical efficiencies are averaged.

Since all these computations are AD-compatible, the gradients of the FoM with respect to the design parameters of each voxel in the structure can be efficiently obtained through AD. These gradients are then propagated backward, as indicated by the red arrows in Figure 2, enabling iterative parameter updates. We employ a stochastic gradient ascent (SGA) to update the design parameters and progressively enhance the structure's performance. The evolution of the structure across iterations is explored in Figure S1 (Supporting Information), providing further insights into the optimization process. Both optimization and verification are based on the RCWA with a Fourier truncation order of.<sup>[8]</sup> Additionally, as shown in Figure S2 (Supporting Information), the structure

is further validated using higher truncation orders up to,<sup>[15]</sup> confirming that the results are identical.

### 3. Result

Figure 1 presents the fully binarized optimized structure, along with its cross-section, which is optimized for  $\theta_t = 12^\circ$  and  $N_L = 100$  layers. The dark cubes represent  $\text{Si}_3\text{N}_4$ , while the light cubes represent  $\text{SiO}_2$ . To compare the proposed broad-angle optimization ( $\theta_t = 12^\circ$ ) with the optimization only at a normal incidence, we analyzed the  $S_z$  distributions of the resulting devices from the two optimizations, as shown in Figure 3a. At normal incidence, both optimized structures exhibit a clear Bayer-shaped RGB field distribution. However, the performance of the normal-incidence-optimized design collapses entirely under  $\pm 12^\circ$  incident angles, failing to maintain the color routing functionality. In contrast, the broad-angle-optimized structure maintains a distinct Bayer-patterned RGB field even at  $\pm 12^\circ$ , demonstrating high color routing efficiency and angular robustness.

To further investigate the influence of the  $\theta_t$  on the proposed design method beyond the specific comparison shown in Figure 3a, we conducted various optimizations, each under

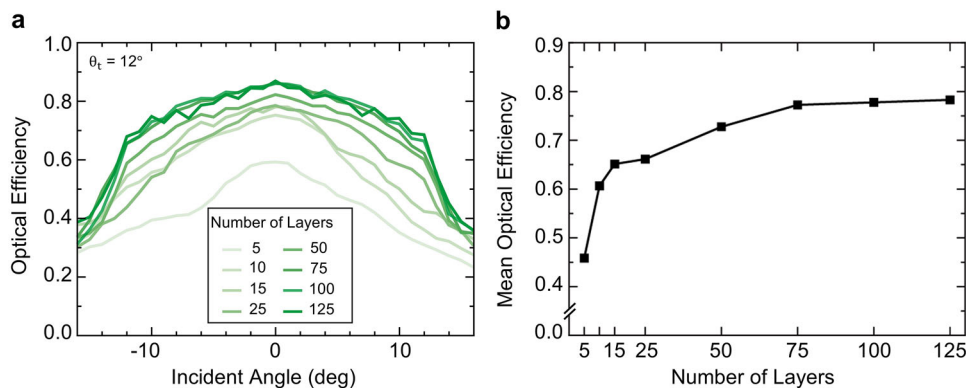


**Figure 4.** Impact of the number of layers. a) The average of RGB optical efficiencies of optimized structures for different  $N_L$ . b) The mean optical efficiency within the  $\pm\theta_i$  range of the incident angle.

different  $\theta_i$  conditions, keeping all other design parameters constant while gradually increasing  $\theta_i$  from  $0^\circ$  to  $20^\circ$  in  $4^\circ$  increments. Figure 3b provides a quantitative analysis of the average RGB optical efficiencies of the optimized color routers for each  $\theta_i$ . The structure designed only for normal incidence (i.e.,  $\theta_i = 0^\circ$ ) achieves near-perfect optical efficiency under that condition. However, the performance drastically drops to  $\approx 29\%$  at  $12^\circ$  oblique incidence, clearly demonstrating its limitation. A similar trend can be found for the other  $\theta_i$  values. Although the optical efficiency at normal incidence of broad-angle-optimized structure (87%) is slightly lower compared to that of normal-incidence-optimized design (99%), it maintains a minimum of 68% of optical efficiency with significantly reduced degradation across the optimized angular range. A similar trend is observed in optical crosstalk, as shown in Figure S6 (Supporting Information). At  $\theta_i = 0^\circ$  case, the crosstalk is almost negligible at normal incidence, but it increases significantly as the angle of incidence increases. Specifically, for the normal-incidence design, the average crosstalk within the  $-12^\circ$  to  $12^\circ$  range is  $\approx 26.8\%$ . However, for the design optimized at  $\theta_i = 12^\circ$ , the crosstalk is significantly reduced, with an average value of only 12%, demonstrating the optimization's ability to reduce crosstalk even at oblique angles. These results emphasize that the methodology proposed in this study is essential to ensure consistently high performance across a broad angular range. The expanded analysis for a broader range of  $\theta$  is provided in Section S7 (Supporting Information). To ensure robust performance across general incident light conditions, we further evaluated the response at intermediate azimuthal angles ( $\varphi = 15^\circ, 30^\circ$ , and  $45^\circ$ ), confirming that the associated optical performance degradation is as low as 9.3% on average at  $\varphi = 45^\circ$ . This validation is provided in Section S5 (Supporting Information) for further details.

We note that as the  $\theta_i$  increases, a trade-off emerges between the angular tolerance and the optical efficiency of the optimized structures. Figure 3c presents the trade-off behavior based on the data shown in Figure 3b, demonstrating that as  $\theta_i$  increases, the half width at half maximum (HWHM) angle increases, while the mean optical efficiency within the  $\pm\theta_i$  range decreases. As  $\theta_i$  increases from  $0^\circ$  to  $20^\circ$ , the mean optical efficiency within  $\theta \in [-\theta_i, +\theta_i]$  decreases from 99% to 67%, while the HWHM increases from  $5^\circ$  to  $20^\circ$ . Figure S3 (Supporting Information) offers further insight into the mechanism behind broad-angle function-

ality by presenting the electric field intensity distributions across the design region. The optimized structures for each  $\theta_i$  are presented in Figure S4 (Supporting Information).

These angular performance trade-offs inherently depend on the structural degrees of freedom. In particular, the number of layers ( $N_L$ ) plays a key role in achieving angular robustness. The impact of  $N_L$  is examined by optimizing structures with  $N_L$  ranging from 5 to 125, while keeping the  $\theta_i$  and the design height fixed at  $12^\circ$  and  $2\ \mu\text{m}$ , respectively. As shown in Figure 4a, increasing  $N_L$  leads to a consistent enhancement in optical efficiency within the incident angle range of  $\pm 12^\circ$ , with the angular response becoming more balanced between positive and negative angles. When  $N_L$  is 5, the optimized structure fails to achieve a meaningful color routing functionality in the full angle range. However, performance improves rapidly as  $N_L$  reaches 10, at which point the structure achieves over 60% mean optical efficiency as shown in Figure 4b. The mean optical efficiency saturates at  $\approx 78\%$  when the  $N_L$  reaches 75, with no noticeable improvement observed at higher  $N_L$ . Figure S7 (Supporting Information) shows that the optical crosstalk exhibits a similar trend. When  $N_L = 5$ , the mean optical crosstalk within the incident angle range of  $\pm 12^\circ$  is 30.4%, but it rapidly decreases as  $N_L$  increases and eventually saturates at  $\approx 12\%$  when  $N_L$  exceeds 75. This indicates that the performance of the router has a limit when increasing the  $N_L$  while maintaining the total height of the design region.

We provide an extended analysis of fabrication constraints in Section S8 (Supporting Information). We first analyze the impact of the minimum feature size (MFS) under the condition of  $N_L = 100$  and  $\theta_i = 12^\circ$ . As shown in Figure S10 (Supporting Information), the design maintains its angular robustness and color routing functionality up to MFS = 50 nm, sustaining an average optical efficiency of 67.8% within the incident angle range of  $\pm 12^\circ$ , while losing its functionality at MFS = 100 nm. Separately, to explore the trade-off between structural simplicity and optical performance, we apply Gaussian filters with different standard deviation ( $\sigma$ ) values to the optimized structure with MFS = 20 nm,  $N_L = 100$ , and  $\theta_i = 12^\circ$ . Figure S11 (Supporting Information) shows that the structure achieves an average efficiency of  $\approx 59\%$  within angular range of  $\pm 12^\circ$ , even with  $\sigma = 60$  nm. In addition, fabrication tolerance is further examined by modeling probabilistic layer misalignments. Figure S13 (Supporting Information) shows that our design remains robust under random

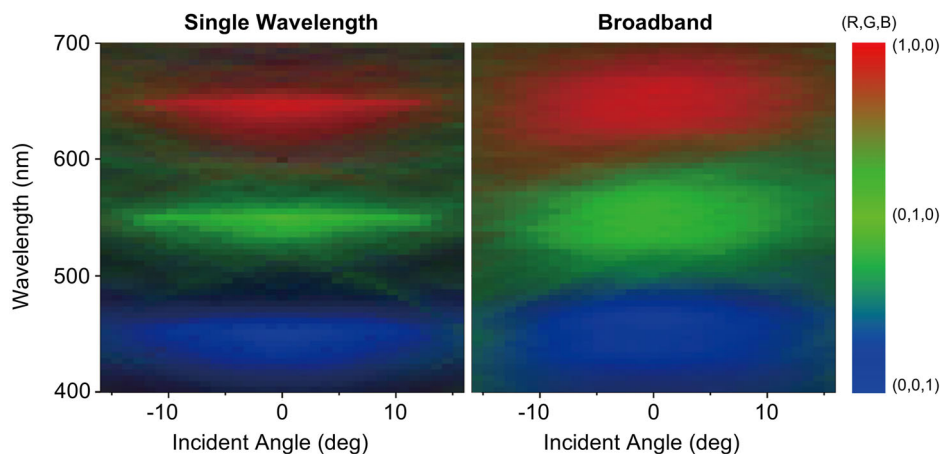


**Figure 5.** Performance of the color router optimized with broadband conditions. Performance of the color router optimized with single wavelength and broadband conditions, for each R, G, and B spectral range. Each heatmap maps the optical efficiency values of the R, G, and B subpixels to their respective color channels using a normalized colormap with RGB values defined in the [0, 1] range.

lateral displacements, where each layer is independently shifted in the  $\pm x$  and  $\pm y$  directions with equal probability. Figure S14 (Supporting Information) illustrates the case of Gaussian-distributed probabilistic shifts, confirming that the design maintains robustness up to  $\sigma = 60$  nm. Moreover, Figure S12 (Supporting Information) shows that a simplified two-layer color router filtered with  $\sigma = 15$  nm achieves an average efficiency of 43.7% within  $\pm 12^\circ$ , outperforming conventional absorptive color filters.

While the previous analysis focused on angular performance at the RGB center wavelengths, real-world applications require stability across broader spectral ranges. To address this, the optimization process is extended to include additional wavelengths around each RGB center. Specifically, the minimax algorithm is modified to incorporate  $\pm 10$  and  $\pm 20$  nm offsets in each iteration. Here,  $\theta_i$  is fixed at  $12^\circ$ , and  $N_L$  is set to 100. Figure 5 presents the performance of the optimized structure as a function of wavelength and incident angle, where the RGB optical efficiencies are mapped to image source values corresponding to each incident condition. The structure optimized under a single-wavelength condition exhibits high performance at each center wavelength but quickly degrades as the wavelength shifts. In contrast, the structure optimized under a multiwavelength condition maintains relatively lower optical efficiency across a broader wavelength-incident angle pair range, demonstrating a trade-off between two variables. The trade-off arising from maintaining high performance across a broad spectral range is particularly evident as the incident angle increases, as shown in Figure S15 (Supporting Information). We also compare the optical crosstalk of the color routers optimized under single-wavelength and broadband conditions, as shown in Figure S16 (Supporting Information). Both the center-wavelength and spectrally averaged results exhibit only minor differences between the two cases, indicating that the two optimization approaches have a minor impact on crosstalk.

#### 4. Conclusion

In conclusion, we propose color routers that are robust to oblique incidence, achieving a balanced trade-off between peak efficiency

and angular robustness. The optimized structure maintains a mean optical efficiency of 78% within a  $\pm 12^\circ$  incident angle range and achieves 87% efficiency under normal incidence, compared to 99% for a normal-only design. While this represents a reduction in peak performance, it is a necessary and acceptable compromise to achieve angular stability, which is essential for real-world imaging conditions. Additionally, we analyze the impact of the target acceptance angle and the number of layers on device performance, thereby outlining the empirical performance boundary of the proposed design strategy. Importantly, we begin by demonstrating that the normal-incidence-optimized structure suffers from severe angular performance degradation, highlighting the necessity of the present study. Finally, by introducing a color router that maintains angular robustness over a broad spectral range, we take a step toward realizing nanophotonic color routers that operate reliably under general incident light conditions. To further assess the practical applicability of the proposed approach, experimental validation through device fabrication is necessary. In addition, accounting for inter-pixel crosstalk between adjacent pixels can further improve the imaging quality of integrated systems. Recently, Lee et al. suggested that thin metallic walls or air trenches could effectively suppress the inter-pixel crosstalk.<sup>[42]</sup>

#### Supporting Information

Supporting Information is available from the Wiley Online Library or from the author.

#### Acknowledgements

This research was supported by the MOTIE (Ministry of Trade, Industry & Energy) 1415180303 and KSRC (Korea Semiconductor Research Consortium) 20019357 support program for the development of the future semiconductor device and also supported by Culture, Sports and Tourism R&D Program through the Korea Creative Content Agency grant funded by the Ministry of Culture, Sports and Tourism in 2024 (RS-2024-00332210) and National Research Foundation of Korea (NRF) grants funded by the Ministry of Science and ICT, Republic of Korea (RS-2024-00414119 and RS-2024-00416583).

## Conflict of Interest

The authors declare no conflict of interest.

## Author Contributions

J.J. and C.P. contributed equally to this work. J.J., C.P., and M.S.J. conceived the ideas. J.J., C.P., and D.H. performed gradient descent optimization computations. J.J. and C.P. conducted a detailed analysis of the optimized structure and its performance. H.C. provided additional guidance. The manuscript was mainly written by J.J., C.P., and M.S.J. with the contributions of all authors. M.S.J. supervised the project.

## Data Availability Statement

The data that support the findings of this study are available from the corresponding author upon reasonable request.

## Keywords

automatic differentiation, image sensors, inverse design, metasurfaces, nanophotonic color router

Received: June 2, 2025

Revised: November 5, 2025

Published online: December 17, 2025

- [1] E. Gamal, H. Eltouky, *IEEE Circuits Devices Mag.* **2005**, 21, 6.
- [2] M. Yako, Y. Yamaoka, T. Kiyohara, C. Hosokawa, A. Noda, K. Tack, N. Spoooren, T. Hirasawa, A. Ishikawa, *Nat. Photonics* **2023**, 17, 218.
- [3] F. Yesilkoy, E. R. Arvelo, Y. Jahani, M. Liu, A. Tittl, V. Cevher, Y. Kivshar, H. Altug, *Nat. Photonics* **2019**, 13, 390.
- [4] D. M. Kita, B. Miranda, D. Favela, D. Bono, J. Michon, H. Lin, T. Gu, J. Hu, *Nat. Commun.* **2018**, 9, 4405.
- [5] Z. Wang, A. Berbillé, Y. Feng, S. Li, L. Zhu, W. Tang, Z. L. Wang, *Nat. Commun.* **2019**, 10, 130.
- [6] T.-H. Hsu, Y.-R. Chen, R.-S. Liu, C.-C. Lo, K.-T. Tang, M.-F. Chang, C.-C. Hsieh, *IEEE J. Solid-State Circuits* **2020**, 56, 1588.
- [7] M. Ishikawa, K. Ogawa, T. Komuro, I. Ishii, presented at *IEEE Int. Solid-State Circuits Conf. Digest of Technical Papers. ISSCC*, San Francisco, CA, USA, February **1999**.
- [8] B. Yuan, S. Chang, G. Liu, L.-Y. Wu, *Chin. J. Mech. Eng.* **2018**, 31, 30.
- [9] I.-M. Park, K. W. Lee, J.-H. Park, S. J. Song, T. Y. Kim, Z. Wu, presented at *2023 Int. Electron Devices Meeting (IEDM)*, San Francisco, CA, USA, December **2023**.
- [10] Q. Chen, X. Nan, M. Chen, D. Pan, X. Yang, L. Wen, *Adv. Mater.* **2021**, 33, 2103815.
- [11] C. Park, S. Lee, T. Lee, J. Kang, J. Jeon, C. Park, S. Kim, H. Chung, M. S. Jang, *J. Opt.* **2024**, 26, 093002.
- [12] S. J. Xiong, X. G. Yang, *Nanoscale* **2024**, 16, 9284.
- [13] H. J. Chung, Z. G. Zhou, P. Bermel, *Appl. Phys. Lett.* **2017**, 110, 201111.
- [14] P. Camayd-Muñoz, C. Ballew, G. Roberts, A. Faraon, *Optica* **2020**, 7, 280.
- [15] P. B. Catrysse, N. Zhao, W. Jin, S. Fan, *Nanophotonics* **2022**, 11, 2381.
- [16] N. Zhao, P. B. Catrysse, S. H. Fan, *Adv. Photonics Res.* **2021**, 2, 2000048.
- [17] M. Miyata, N. Nemoto, K. Shikama, F. Kobayashi, T. Hashimoto, *Optica* **2021**, 8, 1596.
- [18] B. H. Chen, P. C. Wu, V.-C. Su, Y.-C. Lai, C. H. Chu, I. C. Lee, J.-W. Chen, Y. H. Chen, Y.-C. Lan, C.-H. Kuan, D. P. Tsai, *Nano Lett.* **2017**, 17, 6345.
- [19] M. Miyata, M. Nakajima, T. Hashimoto, *ACS Photonics* **2019**, 6, 1442.
- [20] X. Yang, S. Xiong, F. Tan, Z. Lin, Y. Bao, L. Wen, Q. Chen, B. Li, arXiv preprint **2024**, arXiv:2409.12459.
- [21] C. Kim, J. Hong, J. Jang, G.-Y. Lee, Y. Kim, Y. Jeong, B. Lee, *Sci. Adv.* **2024**, 10, adn9000.
- [22] J. Li, Q. Zhang, H. Yang, T. Lei, L. Du, X. Wang, J. Bu, Q. Chen, Y. Liu, Z. Xie, X. Yuan, *ACS Photonics* **2022**, 9, 2607.
- [23] B. Li, A. Deng, K. Li, Y. Hu, Z. Li, Y. Shi, Q. Xiong, Z. Liu, Q. Guo, L. Zou, H. Zhang, M. Zhang, F. Ouyang, J. Su, W. Su, J. Xu, H. Lin, J. Sun, J. Peng, H. Jiang, P. Zhou, T. Hu, M. Luo, Y. Zhang, J. Lu, *Nat. Commun.* **2022**, 13, 460.
- [24] S. Kim, C. Park, S. Kim, H. Chung, M. S. Jang, *IScience* **2023**, 26, 107788.
- [25] G. Roberts, C. Ballew, T. Zheng, J. C. Garcia, S. Camayd-Muñoz, P. W. C. Hon, A. Faraon, *Nat. Commun.* **2023**, 14, 2768.
- [26] Y. Shao, S. Guo, R. Chen, Y. Dang, Y. Zhou, Y. Wang, J. Zhan, J. Yu, B.-F. Ju, Y. Ma, *Laser Photonics Rev.* **2023**, 17, 2300027.
- [27] J. Park, S. Kim, D. W. Nam, H. Chung, C. Y. Park, M. S. Jang, *Nanophotonics* **2022**, 11, 1809.
- [28] C. Kang, C. Park, M. Lee, J. Kang, M. S. Jang, H. Chung, *Nanophotonics* **2024**, 13, 3765.
- [29] P. B. Catrysse, S. H. Fan, *Appl. Phys. Lett.* **2023**, 123, 261105.
- [30] N. A. Switz, M. V. D'Ambrosio, D. A. Fletcher, *PLoS One* **2014**, 9, 95330.
- [31] C. Choi, J. Park, Y. Lee, B. Kim, J. Kim, S. Kim, presented at *2023 Int. Electron Devices Meeting (IEDM)*, San Francisco, CA, USA, December **2023**.
- [32] M. Khorasaninejad, W. T. Chen, R. C. Devlin, J. Oh, A. Y. Zhu, F. Capasso, *Science* **2016**, 352, 1190.
- [33] M. Mitchell, *An Introduction to Genetic Algorithms*, MIT Press, Cambridge, Massachusetts **1998**.
- [34] J. Kennedy, R. Eberhart, *Proc. of ICNN'95 - Int. Conf. on Neural Networks*, Perth, WA, Australia, November **1995**.
- [35] R. J. Tang, S. W. D. Lim, M. Ossiander, X. Yin, F. Capasso, *ACS Photonics* **2023**, 10, 4140.
- [36] M. Minkov, I. A. D. Williamson, L. C. Andreani, D. Gerace, B. Lou, A. Y. Song, T. W. Hughes, S. Fan, *ACS Photonics* **2020**, 7, 1729.
- [37] A. Paszke, S. Gross, S. Chintala, G. Chanan, E. Yang, Z. DeVito, Z. Lin, A. Desmaison, L. Antiga, A. Lerer, *Automatic Differentiation in Pytorch, NIPS 2017 Workshop on Autodiff* **2017**.
- [38] L. B. Rall, *Automatic Differentiation: Techniques and Applications*, Springer, Berlin, Germany **1981**.
- [39] I. H. Malitson, *J. Opt. Soc. Am.* **1965**, 55, 1205.
- [40] H. R. Philipp, *J. Electrochem. Soc.* **1973**, 120, 295.
- [41] Y. Kim, A. W. Jung, S. Kim, K. Octavian, D. Heo, C. Park, J. Shin, S. Nam, C. Park, J. Park, S. Han, J. Lee, S. Kim, M. S. Jang, C. Y. Park, arXiv preprint **2024**, arXiv:2406.12904.
- [42] S. Lee, J. Hong, J. Kang, J. Park, J. Lim, T. Lee, M. S. Jang, H. Chung, *Nanophotonics* **2024**, 13, 3895.